IEEE Photonics Journal
An IEEE Photonics Society Publication

Numerical Study of the Near-Field and Far-Field Properties of Active Open Cylindrical Coated Nanoparticle Antennas

Volume 3, Number 6, December 2011

Junping Geng
Richard W. Ziolkowski
Ronghong Jin
Xianling Liang

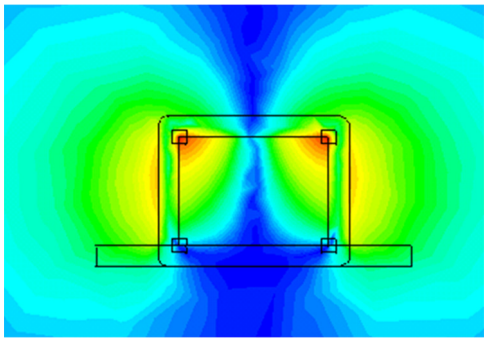

DOI: 10.1109/JPHOT.2011.2173759
1943-0655/$26.00 ©2011 IEEE

IEEE photonics SOCIETY

IEEE

Numerical Study of the Near-Field and Far-Field Properties of Active Open Cylindrical Coated Nanoparticle Antennas

Junping Geng,[1,2] Richard W. Ziolkowski,[2] Ronghong Jin,[1] and Xianling Liang[1]

[1]Electronic Engineering Department, Shanghai Jiao Tong University, Shanghai 200240, China
[2]Department of Electrical and Computer Engineering, University of Arizona, Tucson, AZ 85721 USA

DOI: 10.1109/JPHOT.2011.2173759
1943-0655/$26.00 ©2011 IEEE

Manuscript received August 27, 2011; revised October 21, 2011; accepted October 21, 2011. Date of publication October 27, 2011; date of current version November 14, 2011. This work was supported in part by "973" (2009CB320403); the Natural Science Foundation of Shanghai (10ZR1416600); the Doctoral Fund of Ministry of Education of China (20090073120033); the National Science and Technology of major projects (2011ZX03001-007-03); the National Science Fund for Creative Research Groups (60821062); the Scientific Research Foundation for Returned Scholars, Ministry of Education of China; and by the Office of Naval Research under Contract H940030920902. Corresponding author: J. Geng (e-mail: gengjunp@gmail.com).

Abstract: A very electrically small, active open cylindrical coated nanoparticle model is constructed, and its electromagnetic properties are investigated in the visible frequency band. Its optical response under both planewave and electric dipole antenna excitations shows very strong dipole behavior at its lowest resonance frequency. The scattering cross section at that dipole resonance frequency is increased by more than $+50$ dBsm for the planewave excitation. When the open structure is excited by a small current $(I0 = 1 \times 10^{-3}\ \mathrm{A})$ driven dipole antenna, the maximum radiated power of the composite nanoantenna can be increased by $+83.35$ dB over its value obtained when the dipole antenna radiates alone in free space. The behaviors under various locations and orientations of the dipole are explored. Dipole orientations along the cylinder axis and symmetric locations of the dipole produced the largest radiated power enhancements.

Index Terms: Electrically small antennas, metamaterials, nanoantenna, nanostructures, plasmonics, radiation, scattering.

1. Introduction

Nanoparticles and nanostructures have been shown to have attractive prospects for advancements in the areas of metamaterials [1], [2], biology and medicine [3], [4], efficient solar cells [5]–[7], and high resolution imaging [8]–[10]. They have even been considered as sensor realizations that could provide noninvasive measurements of the electromagnetic properties of molecules or other nanoparticles [11]–[13]. Because of the surface plasmon characteristics realized by combining metals at optical frequencies, which acquire epsilon negative (ENG) properties, with normal dielectrics, which have double positive (DPS) properties, one can design nanosized resonant particles that could be used to achieve highly sub-wavelength lasing elements and nanoamplifiers [14], [15]. Moreover, it has been demonstrated that subwavelength metallic coated nanoparticles (CNPs), i.e., plasmonic spherical shell nanoparticles, which consist of spherical dielectric cores surrounded by spherical metal nanoshells, can lead to novel nanoantenna properties, including resonant radiated power enhancements and resonant jamming effects [17], [18].

If the dielectric of the CNP is lossless or lossy, the system will be called a *passive CNP*. Passive CNPs exhibit geometric tunability [19]; they have been synthesized and their behaviors have been verified experimentally [20]. The tunability of their CNP resonances is a desirable characteristic for a number of applications. On the other hand, if gain material is included in the dielectric, it will be called an *active CNP*. Active CNP-based nanoamplifiers and nanolasers have been studied [14], [15]. In particular, it was demonstrated that the intrinsic losses present in the plasmonic materials can be overcome. Experimental verification of some of these active properties was reported recently [21].

Losses remain one of the main disadvantages of using metals at optical frequencies. They constrain the possible enhancements of the resonant, passive CNPs. Consequently, gain material was introduced into the CNPs to overcome those losses and to enhance their resonant responses [14], [17]. Different metal coatings exhibit analogous but distinct resonant behaviors [18]. In the visible regime, silver remains the lowest loss candidate for CNP related applications. It will be emphasized in the configurations reported below. Several different gain materials have been considered. Initially, to explore a configuration and its potential usefulness, the core media generally is selected to be a canonical gain medium, i.e., one simply specified by the real and imaginary parts of its refractive index, i.e., as $(n - j\kappa)$. More realistic materials also have been suggested. For instance, because of their extensive use in optical fibers (e.g., [22]), three-level models of Er^{3+} molecules were considered. Quantum dots have been championed for related plasmonic-based nanolasers, i.e., SPASERs [15], [23]. Dyes have led to the first actual experiments [18], [21]. We will use the canonical gain model in the studies reported below.

When either the passive or active CNP is illuminated by a planewave, its performance can be expressed in terms of its absorption cross section (ACS), scattering cross section (SCS), and extinction cross section (ECS), all of which depend on the radius of the dielectric core and the thickness of the metal shell, e.g., Electric Hertzian dipole (EHD) sources are another form of excitation that has been considered [17]–[19]. The radiated power ratio (PR), i.e., ratio of the total power radiated in the presence of the CNP to its value generated in free space, has been a useful figure of merit for the EHD excitations. For either excitation mechanism, specific passive and active CNP-based nanoantennas have been designed to be resonant, leading to much larger values of their radiated powers. The EHD is assumed to be a fluorescing molecule/atom that is excited by another field at a frequency different from the transition frequency at which its dipole moment is established. Because the resonances are very narrow band, the active CNP would have minimal impact on the original exciting field and its creation of the EHD. Then the traditional approach of impedance matching to the source is replaced by the coupling efficiency of the assumed fluorescing molecule/atom to the active CNP at the transition frequency, i.e., the accepted power delivered to the active CNP results from matching its design to the EHD. The radiated PR is the most relevant parameter to quantify the effectiveness of this EHD coupling to this nanoamplifier and the performance of the resulting nanoantenna.

Besides the CNP-based dipole radiator, a variety of other nanoantenna structures has been investigated over the past few years [25]–[36]. This includes optical dipoles [37]–[40], monopoles [41], [42] and several types of "gap" antennas [43]–[45]. All of these antennas exhibit approximately a dipolar angular emission, i.e., their modes both radiate and are excited with a dipolar angular dependence. Optical nanodimers have been analyzed, e.g., [46]. Because of the resulting spreading of the displacement current in the nanodimer gap, this two-nanoparticle configuration may provide a larger radiation efficiency and resonance tunability than with other optical nanodipoles. An optical Yagi–Uda nanoantenna was proposed in [47] with near-field coupling being used to feed the element at the resonance frequency. The resonant plasmon mode of this antenna determines the angular emission of the coupled system. Bowtie antennas [48] combine scattering from their component arms to form a strong hot spot in their gap. Their resonances are simply tuned by their sizes. Bowtie antennas recently have been used as near-field probes and for nanolithography [48], [49]. A cylindrical metal shell having a metal top and being filled with silicon nitride and InGaAs layers was investigated experimentally in [50]. These results indicate the possibility of a good fabrication method for constructing pillar-like nanostructures.

Theoretical analyses have been used to derive the characteristics of many of these optical nanoantennas, particularly those such as the canonical-shaped spherical CNPs. These often analytical or semianalytical obtained results have shown attractive performance characteristics for many of the aforementioned nanoantennas. Unfortunately, canonical geometries are idealized structures and can be far from practical realization with existing fabrication technologies. There are more complicated nanostructures which may be more suitable in that sense. Moreover, there should be questions whether their intriguing enhancements will also occur for more complex nanoantennas. In this paper, we numerically characterize the near-field and far-field scattering and radiation characteristics of one such noncanonical configuration. In particular, we will emphasize active open cylindrical CNPs (AOC-CNPs) that are excited by both planewaves and EHDs. We begin in Section 2 by explaining how we adapted a commercial computational electromagnetics (CEM) solver to these active material problems. The planewave scattering and EHD excitation properties of the AOC-CNPs are examined, respectively, in Sections 3 and 4. In contrast to the closed spherical CNPs, which are realizable with chemistry approaches, the open pillar-like AOC-CNP geometry may be more amenable to other standard nanofabrication processes. It will be shown that as with the closed canonical geometries, several AOC-CNP configurations can be designed to be highly resonant, producing very large SCSs and radiated PRs, both stemming from basic dipole modes and having strong linear polarization characteristics. The PRs for the AOC-CNPs excited by the both vertical and horizontal EHDs are studied. Variances in the material parameters and the AOC-CNP geometries lead to optimized designs. While the symmetric AOC-CNP configurations are emphasized, an asymmetric version is considered in Section 5. It is shown that it too can produce similar enhanced near- and far-field properties. Conclusions are given in Section 6.

2. Numerical Models

2.1. Background

Once the basic operating principles of a canonical structure has been identified, more realistic, complex design problems can only be analyzed with CEM tools. These include commercial EM software packages such as CST Microwave Studio, COMSOL Multiphysics, and ANSYS/ANSOFT HFSS. CST MICROWAVE STUDIO is a CEM simulation tool set which solves Maxwell's equations in the time domain based on the finite integration in time (FIT) technique (a slight generalization of the finite-difference time-domain (FDTD) method), as well as in the frequency domain with the finite-element method (FEM) [51], [52]. For wide bandwidth problems, time domain methods are a good choice. On the other hand, frequency domain methods are generally more appropriate for narrow band problems. In addition to providing both time and frequency domain simulation capabilities, the CST software tools also have a user-friendly interface and a powerful postprocessing environment that allows one to tailor the output results. All of the simulation results described here were obtained with this software.

2.2. Dispersive Material Models

With any lossy real or artificial material, dispersive effects must be taken into account. This is especially true of all ENG, mu-negative (MNG), and double negative (DNG) and DPS metamaterials. The lack of general purpose dispersion models was a drawback of former versions of CST. However, in recent versions, CST has added some functionality that allows one to model frequency dependent, passive negative permittivity and permeability materials. Unfortunately, there are some difficulties yet in the time domain solver for negative conductivity or for obtaining the desired sign of the imaginary part of the refractive index to model active media. Nonetheless, we have found [53] that a user can introduce gain in the frequency domain solver by manipulating the material parameters in the "history list" manually. It is for this reason that this manual process is introduced below to analyze the active CNP problem with the CST software tools. We have confirmed that the CST results obtained in this manner reproduce the analytically obtained ones for the canonical passive and active spherical CNPs.

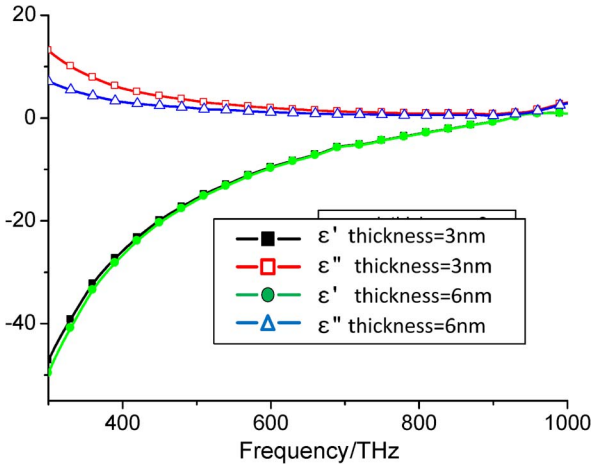

Fig. 1. Permittivity of silver films whose thicknesses are 3 nm and 6 nm.

2.2.1. Optical Material Properties

An improved model of the metal plasmonic shells at optical wavelengths between 200 nm to 1800 nm was given in [14]; it reproduces the empirical values given in [54], [55]. The permittivity is decomposed into a size dependent Drude response and an interband transition response as follows:

$$\varepsilon(\omega, R) = \varepsilon_{Drude}(\omega, R) + \chi_{Interband}(\omega) \tag{1}$$

where the term R taken to be the thickness of the metal shell, and the Drude permittivity is given by the expression

$$\varepsilon_{Drude}(\omega, R) = 1 - \frac{\omega_p^2}{\Gamma(R)^2 + \omega^2} + j\frac{\Gamma(R)^2\omega_p^2}{\omega(\Gamma(R)^2 + \omega^2)} \tag{2}$$

where ω_p and Γ are, respectively, the plasma and the collision frequencies. The size dependence is treated as an effect which arises when the size of the material approaches and becomes smaller than the bulk mean free path length of the conduction electrons in it, i.e., when it is thinner than 100 nm. It is treated as an alteration in the mean free path which is then incorporated into the Drude model through the size dependent damping frequency. In particular, the damping frequency is assumed to take the form

$$\Gamma(R) = \Gamma_\infty + \frac{AV_F}{R} \tag{3}$$

where A is a constant term assumed to be approximately unity, i.e., $A \sim 1$. The term V_F is the Fermi velocity. The Drude parameters and the Fermi velocity values used for silver in our simulations were [14] $m^*/m = 0.96$ and $N = 5.85 \times 10^{28}$ m^{-3}, giving $\omega_p = 1.39269 \times 10^{13}$ s^{-1}, $V_F = 1.39 \times 10^6$ m/s, and $A = 1.0$. Using this process, the permittivities of silver films whose thickness is 3 nm and 6 nm were calculated. The results are shown in Fig. 1.

2.2.2. Active Media in Nanoshells

The core of the passive models of the CNPs studied to date has been filled with silicon dioxide, SiO_2. Because SiO_2 has very low loss characteristics, we can set the relative epsilon to be a constant $\varepsilon_r = 2.05$, yielding the refractive index $n = \sqrt{\varepsilon_r} = 1.432$. However, if the filling media is a higher-loss silica or some other lossy dielectric, the dielectric constant will then include an imaginary part, i.e., $\varepsilon(\omega) = \varepsilon'(\omega) - j\varepsilon''(\omega)$. In particular, when losses are present, the refractive index

TABLE 1
Relationship between the static permittivity and the collision frequency

Γ	$\varepsilon_S=2n\kappa\Gamma/\omega_0+\varepsilon_\infty$	
$10^{-3}\omega_0$	1.98678	
$10^{-2}\omega_0$	1.98034	$n=1.432$
$10^{-1.3}\omega_0$	1.95162	$\kappa=-0.25$ $f_0=600THz$
$10^{-1}\omega_0$	1.91591	$\omega_0=2\pi f_0$

expression contains an imaginary term κ. The permittivity and the real and imaginary parts of the refractive index are then related by the expression

$$\varepsilon_r = (n - j\kappa)^2 = n^2 - \kappa^2 - j2n\kappa. \tag{4}$$

Here, κ is varied over a range of values that represent the expected loss or gain in the core of the nanoshell, where $\kappa > 0$, $= 0$, and < 0, respectively, for a lossy, lossless, and gain medium.

2.2.3. Lorentz Model

To incorporate the canonical gain into CST Microwave Studio, one must consider a *Lorentz model* [56] description of the form

$$\varepsilon_r(\omega) = \varepsilon_\infty + \frac{(\varepsilon_S - \varepsilon_\infty)\omega_0^2}{\omega_0^2 + j\omega\Gamma - \omega^2}. \tag{5}$$

For the spherical, active CNPs with the active SiO_2 core and silver shell studied in (e.g., [17], [18]), an optimal value of $\kappa = -0.25$ was found for excitation frequencies around 600 THz (500-nm wavelength). We elected to use the same gain values in the present study. For the SiO_2 core, we keep $n = \sqrt{\varepsilon_r} = 1.432$ and set $\kappa = -0.25$ at the resonance frequency of the structure. To generate these values from (5), we set $f = f_0 = 600$ THz and $\omega = \omega_0 = 2\pi f_0$ to obtain

$$\varepsilon_r(\omega_0 = 2\pi f_0) = \varepsilon_\infty + \frac{(\varepsilon_S - \varepsilon_\infty)\omega_0}{j\Gamma}. \tag{6}$$

Combining (5) and (6), we then calculated $\varepsilon_\infty = 1.9875$ and $(\varepsilon_S - \varepsilon_\infty)\omega_0/\Gamma = 2n\kappa$ so that

$$\varepsilon_S = \frac{2n\kappa\Gamma}{\omega_0} + \varepsilon_\infty = \frac{2n\kappa\Gamma}{\omega_0} + 1.9875. \tag{7}$$

The remaining value to specify is Γ, the collision frequency (or damping factor). It is frequently related to the resonant frequency for simplicity. We considered it in the range $(10^{-3} \sim 10^{-1})\omega_0$, to represent low to high loss materials. Some values of Γ and the resulting values of ε_s are listed in Table 1 for reference.

Based on the above derivation and the values of its constants, the values of the real and imaginary parts of the Lorentz model of the relative permittivity of the active SiO_2 are shown in Fig. 2. The curves exhibit typical behavior when gain is present in a Lorentz medium. For the following cases, we choose the lower loss value $\Gamma = 10^{-3}\omega_0$.

2.3. Planewave Excitation Performance Terms

To characterize the behavior of a structure being excited by an electromagnetic planewave, one generally considers the SCS and the ACS of that structure. The SCS is defined as the total integrated scattered field power normalized by the irradiance of the incident field. The ACS is defined by the net flux through a surface surrounding the structure normalized by the incident

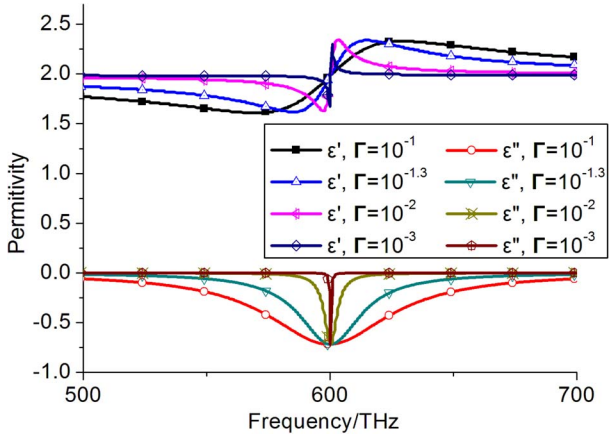

Fig. 2. Permittivity of doped SiO_2 with different Γ at $\omega_0 = 120\pi \times 10^{12}$.

field irradiance. Both the absorption and SCSs can be expressed via Poynting's theorem through the power scattered and absorbed by the structure. The latter are given by the following expressions:

$$P_{scat} = \mathrm{Re}\left\{\frac{1}{2}\iint_S \left[\vec{E}_S \times \vec{H}_S^*\right] \cdot \hat{n}\, dS\right\} \tag{8}$$

$$P_{abs} = -\mathrm{Re}\left\{\frac{1}{2}\iint_S \left[\vec{E}_{tot} \times \vec{H}_{tot}^*\right] \cdot \hat{n}\, dS\right\} \tag{9}$$

where S is a surface that completely surrounds the particle and $\hat{n}$ is the unit outward pointing normal to it. Labeling the incident, scattered, and total fields by the subscripts *inc*, *scat*, and *tot*, respectively, the total SCS, ACS, and ECS are thus defined from the ratio of the scattered or absorbed power to the incident irradiance I_{inc} and can be expressed as

$$\sigma_{scat} = \frac{P_{scat}}{I_{inc}} \tag{10}$$

$$\sigma_{abs} = \frac{P_{abs}}{I_{inc}} \tag{11}$$

$$\sigma_{ext} = \sigma_{scat} + \sigma_{abs}. \tag{12}$$

These quantities are readily calculated with the CST postprocessing tools.

2.4. Radiated Power by Small Current

To characterize the behavior of a structure being excited by an EHD, one considers the total radiated power. It is given by the Poynting's vector-based expression

$$P_{tot} = \lim_{r\to\infty} \frac{1}{2} \int_{\theta=0}^{\pi} \int_{\varphi=0}^{2\pi} \mathrm{Re}\left\{\vec{E}_{tot}(r,\theta,\varphi) \times \vec{H}_{tot}^*(r,\theta,\varphi)\right\} \cdot \hat{n}\, dS \tag{13}$$

where the surface S is taken to be a sphere enclosing the entire nanoantenna system. For an EHD with a dipole current moment $p_s = I_0 d$ radiating in free space, this yields [57, p. 155]

$$P_i = \frac{\eta_0 \pi}{3}\left|\frac{p_s k_0}{2\pi}\right|^2 \tag{14}$$

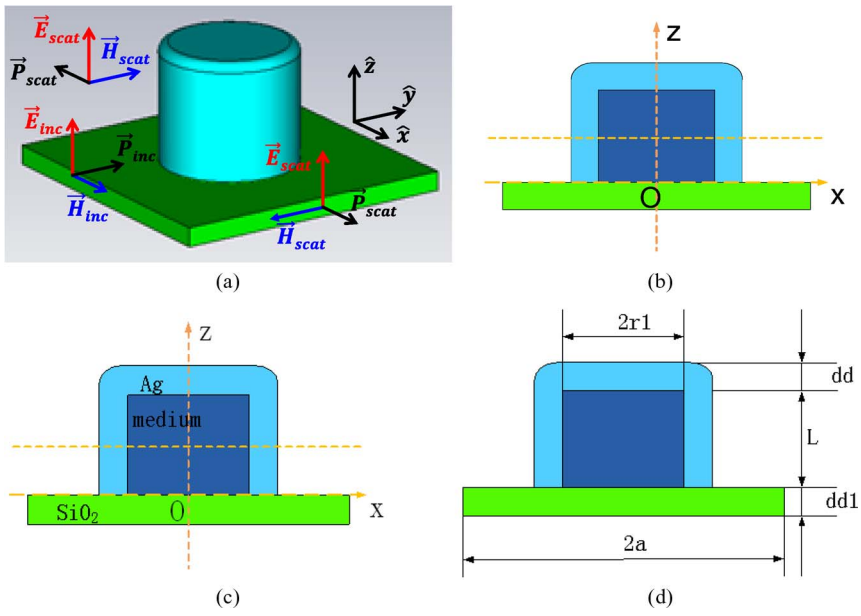

Fig. 3. Open cylindrical coated nanoparticle antenna model. (a) 3-D perspective model. (b) *y*-cut plane. (c) Material components. (d) Dimension and parameters.

where $\eta_0 = 376.7\ \Omega$ is the characteristic impedance of free space. The radiated PR is then defined simply as

$$PR = \frac{P_{tot}}{P_i}. \tag{15}$$

3. Active Open Cylindrical CNP Excited by a Planewave

The noncanonical geometry considered here is the open cylindrical CNP shown in Fig. 3. It consists of either a passive or active cylindrical silica core that is coated on its sides and top with silver, i.e., the silver coating layer forms a cup and is entirely filled with the silica medium. The core is either lossless SiO_2 (passive CNP) or SiO_2 impregnated with gain material (AOC-CNP). This CNP rests its open face on a finite silica slab, the axis of the cylinder being along the normal to the large face of the slab. The coordinate system is shown in the figure. The substrate is taken to be the lossless SiO_2; it is a rectangular slab with dimensions: $2a \times 2a \times dd1$. This would correspond to a silver coating of a simple or gain impregnated silica cylinder grown on a silica slab. We assume that the structure has the fixed height $L = 31.5$ nm, silver thickness $dd = 6.0$ nm, and substrate thickness $dd1 = dd = 6.0$ nm. The silver thickness choice corresponds to the cases considered previously (see, e.g., [14], [17], and [18]) for the active spherical CNP. The SiO_2 substrate is taken to be 90 nm $\times$ 90 nm $\times$ 6 nm. The silver cup forms a nanocavity that is filled with either the passive dielectric or the active gain material.

The entire structure is excited by a vertically polarized planewave, in which the *E* field vector is parallel to the *z*-axis and the propagation direction is along the $+x$-axis. The incident planewave field is explicitly given as

$$\vec{E} = \hat{z}E_0\cos(\omega t - kx). \tag{16}$$

The amplitude of the incident planewave was taken to be $E_0 = 1.0$ V/m.

To determine the resonances of the electrically small, AOC-CNP structure, the CST model was run with the radius $r1$ of the inner cavity being swept from 20 nm to 23 nm. This interval was selected based on our anticipation that the resonance for this open structure would occur for a

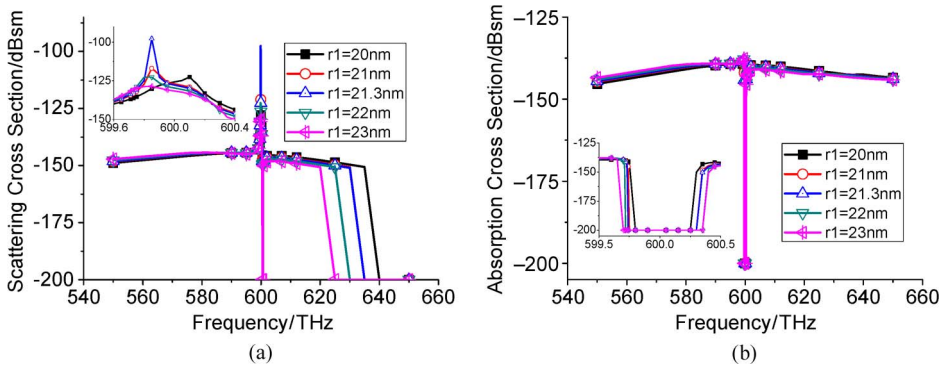

Fig. 4. Cross sections with r1 swept from 20 nm to 23 nm. (a) Scattering cross section and a zoomed-in view near its maximum values. (b) Absorption cross section and a zoomed-in view near its minimum values.

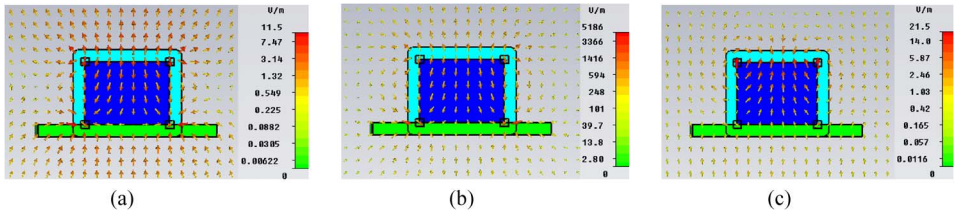

Fig. 5. E-field near the AOC-CNP. (a) $f = 550.0$ THz. (b) $f = 598.85$ THz. (c) $f = 650.0$ THz.

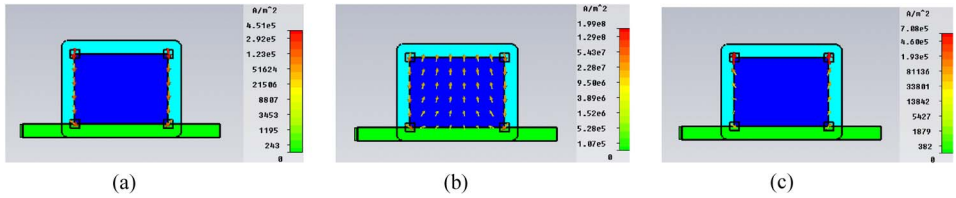

Fig. 6. Current density in the AOC-CNP. (a) $f = 550.0$ THz. (b) $f = 598.85$ THz. (c) $f = 650.0$ THz.

volume somewhat below the (closed) spherical 30-nm outer radius CNP cases treated, for instance, in [14]. The SCS and ACS are shown in Fig. 4. From Fig. 4(a), the optimum parameter value for the AOC-CNP scatterer is found to be $r1 = 21.3$ nm. This structure produces a maximum of the SCS peak: -97.69 dBsm at 599.85 THz. Note that this is more than a 50-dBsm increase over the background values. For all simulated values of $r1$, the SCS peaks are actually close to 600 THz in Fig. 4(a). Similar behavior of the ACS curves is shown in Fig. 4(b). The ACS minimum also occurs at 599.85 THz. Note that the -200 dB floor of the ACS data shown in the subplot of Fig. 4(b) is an artifact of the CST software. Again, the minimum is more than 50 dB below the background value. Both the SCS and ACS values clearly show a significant amplification of the scattered signal, i.e., the AOC-CNP acts as a nanoamplifier, just as the active spherical CNP studied, e.g., in [14] did.

The predicted E-field distributions for the AOC-CNP with $r1 = 21.3$ nm at three excitation frequencies: 550.0 THz, 599.85 THz, and 650.0 THz, are shown in Fig. 5. The significant enhancement of the electric field in the core of the AOC-CNP at resonance is shown in Fig. 5(b). However, because of its electrically small size, the field vectors in all three cases form a dipole distribution as expected. Nonetheless, because the planewave in incident from the left, one can see small asymmetries in the off-resonance distributions. The corresponding enhancement of the current density in the core at resonance is shown in Fig. 6. It is clear from Fig. 6(b) that there are very large

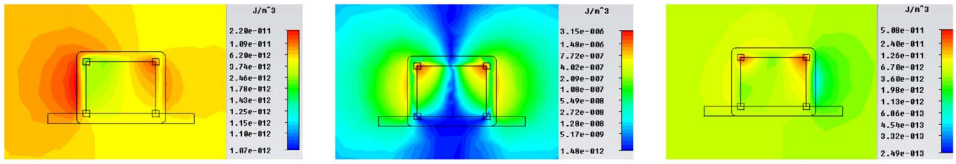

(a) (b) (c)

Fig. 7. Magnetic field energy density near the AOC-CNP. (a) $f = 550.0$ THz. (b) $f = 598.85$ THz. (c) $f = 650.0$ THz.

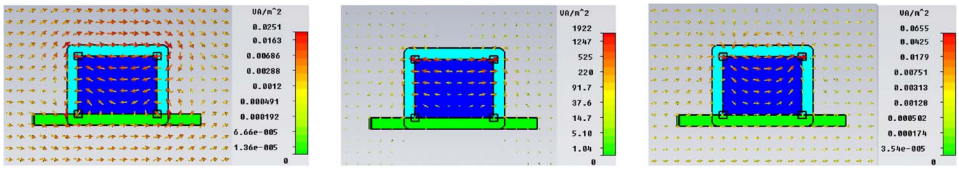

(a) (b) (c)

Fig. 8. Power flow near the AOC-CNP. (a) $f = 550.0$ THz. (b) $f = 598.85$ THz. (c) $f = 650.0$ THz.

currents formed in the core at the resonant frequency when the active medium is present. Off the resonance, the current density is large mainly in the shell region. The corresponding magnetic field energy distributions are shown in Fig. 7. The dipole pattern of the field is again clearly seen at the resonance frequency in Fig. 7(b). Note that the energy distribution at resonance is symmetric about the z-axis but is a bit asymmetrical with respect to the middle of the cylinder. This is due to the open end of the cylinder, i.e., the structure along the z-axis is not symmetric. Finally, the power flow (Poynting vector field) near the AOC-CNP is given in Fig. 8. At resonance, the power is clearly flowing away from the center of the open cavity structure. Moreover, notice that along with the change in sign of the electric field direction within the core, the power flow within the cylinder experiences a sign change as the frequency varies from below to above its resonance value.

4. Active Open Cylindrical CNP Excited by Small Current

Having established the resonance of the AOC-CNP for the planewave excitation, the behavior of the structure under the EHD excitation was examined. This study emphasized how well the AOC-CNP would act as a nanoamplifier and, hence, as a nanosensor for various EHD locations once it was designed based on the planewave excitation. For instance, since a fluorescing atom or molecule would act as a dipole in its transition from an excited to a lower energy state, it was hoped that a resonant AOC-CNP could be designed to amplify significantly the resulting emission signal in whatever location the emitter was relative to the nanoamplifier. Moreover, it was hoped that the silica base could act as a platform to which such fluorescing elements could be attached, further aiding in the localization of the emitter. Consequently, the structural parameters of the planewave excitation-designed AOC-CNP remained the same. The fluorescing emitter was then simulated by specifying a small current element, i.e., an EHD, at the point $[(rx, 0, zc), (rx, 0, zc + 2nm)]$ that was oriented parallel to the z-axis and that had the current moment $I_0 d = 2 \times 10^{-12}$ A-m.

4.1. Horizontal Scan of the EHD Location

The EHD was first located along the substrate interface (at $zc = 0$) at all the positions indicated in Fig. 9, i.e., rx was varied. The predicted PR and ACS values are shown in Fig. 10. The peak of the PR curves in Fig. 10(a) appears at $f = 599.85$ THz. It is 69.12 dB at point C $(rx = -r1 - dd, zc = 0)$. The minimum of the ACS in Fig. 10(b) is found for the same frequency. Consequently, the total radiated power of a dipole placed at the outside edge of the cylinder will be enhanced by more than 69 dB in comparison with its value in free space. The electric field, current density, and power flux distributions at the resonance frequency when the dipole is located at point C

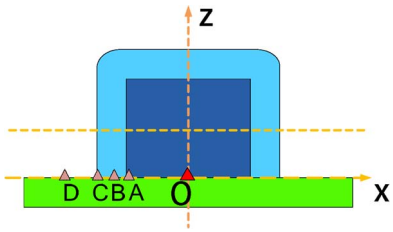

Fig. 9. Horizontal scan of the EHD location along the silica substrate. Simulations were run for a small current source located along the substrate interface (x-axis) at points O, A, B, C, and D.

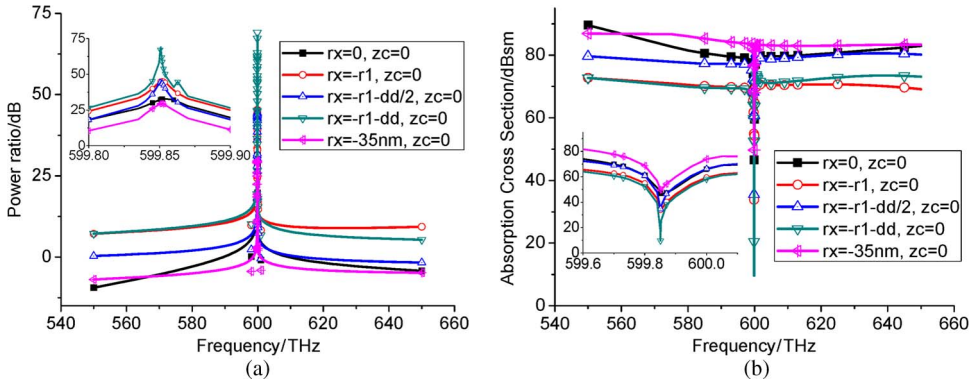

Fig. 10. Power ratio and absorption cross section curves for different dipole locations rx along the x-axis (with $zc = 0$). (a) Power ratio. (b) Absorption cross section.

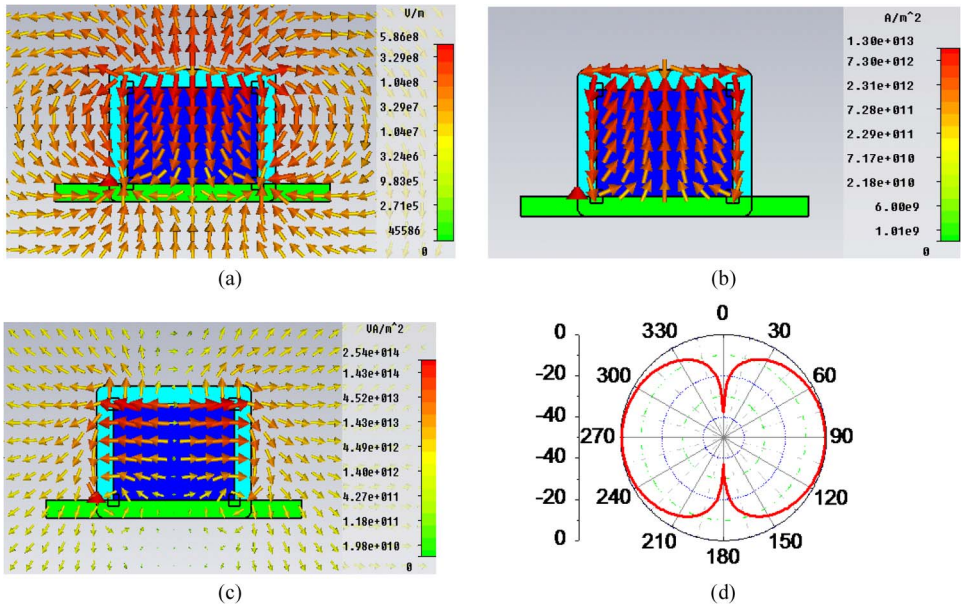

Fig. 11. Simulation results at the resonance frequency of 598.85 THz when the dipole is located at point C. (a) Electric field, (b) current density, (c) power flow, and (d) far field pattern in the $\phi = 0^\circ$ plane.

are shown in Fig. 11. Despite the offset of the EHD, the AOC-CNP still dominates the results; a dipole mode is excited that is symmetrically distributed with respect to the z-axis. This is confirmed with the far-field directivity pattern given in Fig. 11(d). Fig. 11(b) shows again that there are very large

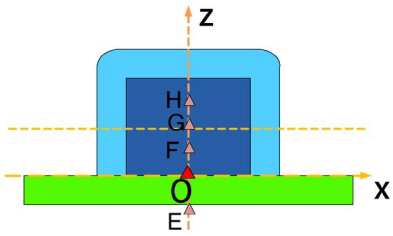

Fig. 12. Vertical scan of the EHD location along the cylinder axis. Simulations were run for a small current source located at points E, O, F, G, and H.

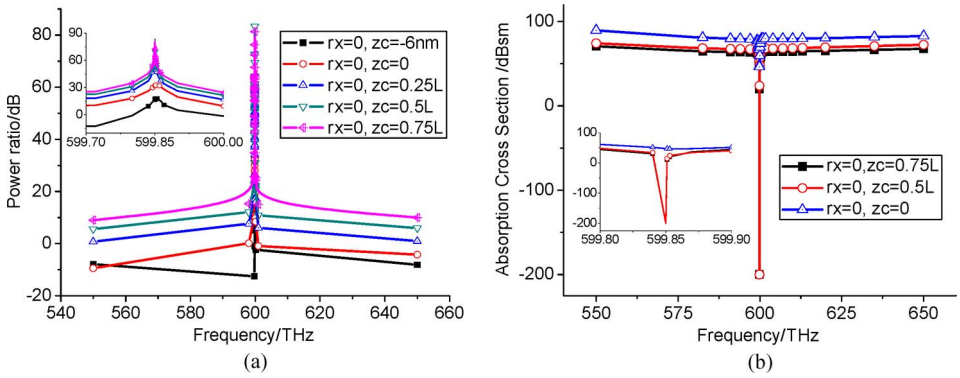

Fig. 13. Power ratio and absorption cross section curves for different dipole locations *zc* along the *z*-axis (with $rx = 0$). (a) Power ratio. (b) Absorption cross section.

currents through the gain medium at the resonant frequency while they are mainly in the shell region away from the resonance frequency. Moreover, the power flow shown in Fig. 11(c) remains strongly outward flowing when the AOC-CNP has gone into resonance.

In contrast to the active closed spherical CNP for which the PR is essentially constant for any interior position of the EHD and only slightly lower for any exterior position near the outer surface [17], the subplot in Fig. 10(a) shows nontrivial decreases in the PR for the points away from point C along the silica slab interface. This location for the maximum response is very advantageous for nanosensor concept of attaching an emitter to the outer surface of the AOC-CNP.

4.2. Vertical Scan of the EHD Location

The EHD was next located along the axis of the cylinder (i.e., at $rx = 0$) at all the positions indicated in Fig. 12, i.e., *zc* was varied. The predicted PR and ACS values are shown in Fig. 13. The peak of the PR curves in Fig. 13(a) appears at $f = 599.85$ THz. It is 83.35 dB at point G $(rx = 0, zc = 0.5L)$. The minimum of the ACS in Fig. 13(b) is again found at the same frequency. Consequently, the total radiated power of a dipole placed inside the cylinder at the middle of the gain medium will be enhanced by more than 83 dB than its value in free space. The electric field, current density and power flux distributions at the resonance frequency when the dipole is located at point G are shown in Fig. 14. Despite the offset of the EHD, a dipole mode is excited that is symmetrically distributed with respect to the *z*-axis and the AOC-CNP behavior dominates the response of the entire nanoantenna system Again, there are very large currents through the gain medium at the resonant frequency while they are mainly in the shell region away from it. Moreover, while there is some variation near the corners of the cylinder, the power flow remains strongly outward flowing when the AOC-CNP has gone into resonance. While there is a significant enhancement of the total radiated power when the EHD is located at point G, a more practical location, again for a nanoamplifier application, is at point E. One could envision molecules at point E on one side of the substrate while the electrically small cavity resonators, i.e., the AOC-CNPs, are

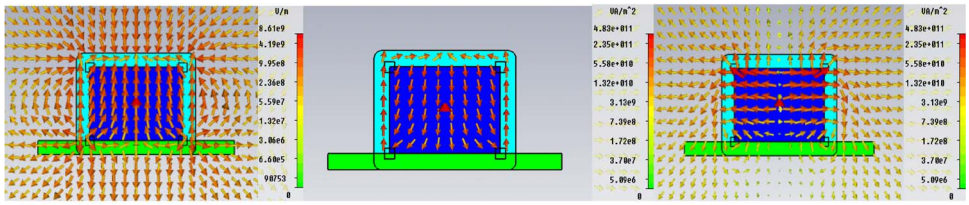

Fig. 14. Simulation results at the resonance frequency 598.85 THz when the dipole is located at point G. (a) Electric field, (b) current density, and (c) power flow distributions.

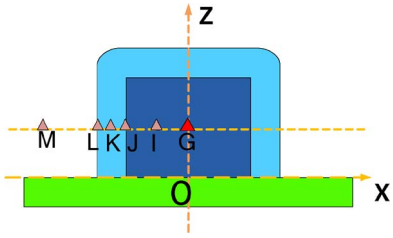

Fig. 15. Horizontal scan of the EHD location when it is displaced along the z-axis to $zc = 0.5L$. Simulations were run for a small current source located at points G, I, J, K, L, and M.

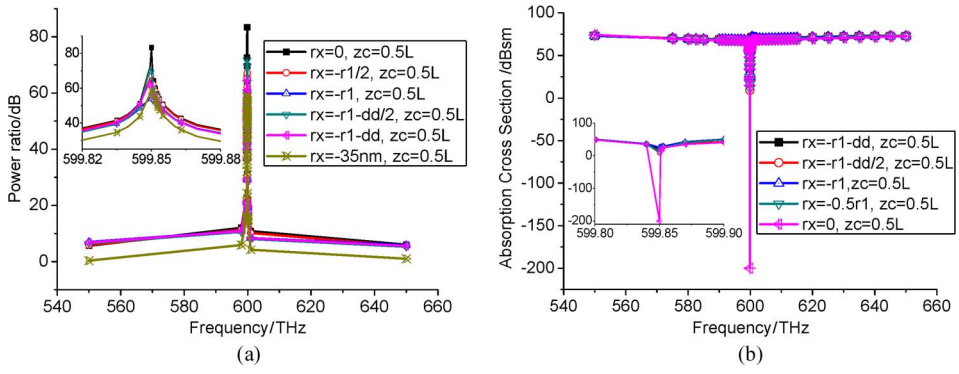

Fig. 16. Power ratio and absorption cross section curves for different dipole locations when $zc = 0.5L$ and rx varies along the x-axis. (a) Power ratio. (b) Absorption cross section.

on the other side. The PR at the resonance frequency is only 18.96 dB, which is considerably smaller value than that obtained at points C or G. Nonetheless, it is still approximately two orders of magnitude larger than in free space. The total power radiated into the far field is enhanced by the presence of the nanoamplifier and, thus, could lead to a desirable measurement configuration on either side of the substrate. Because the PR at point O at the resonance frequency is an order of magnitude larger at 33.00 dB, the overall effect of trenches in the substrate to position a molecule and to bring it closer to the active medium is currently under investigation.

4.3. Horizontal Scan When the EHD Location Is Vertically Displaced

The EHD was next displaced along the axis of the cylinder and located at $zc = 0.5L$. It was then moved to at all the positions, i.e., rx was varied, as indicated in Fig. 15. The predicted PR and ACS values are shown in Fig. 16. The peak of the PR curves in Fig. 16(a) and the minimum of the ACS again appear at $f = 599.85$ THz. It remains 83.35 dB at point G $(rx = 0, zc = 0.5L)$. The value just outside the shell at point L is 64.39 dB, which is approximately the same as it was for point C.

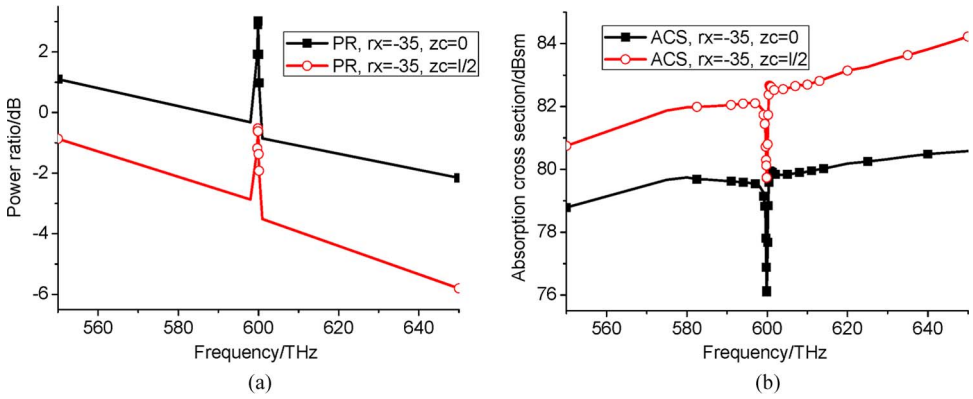

Fig. 17. Comparison of PR and ASC values for the horizontally oriented EHD excitation of the AOC-CNP. (a) PR. (b) ACS.

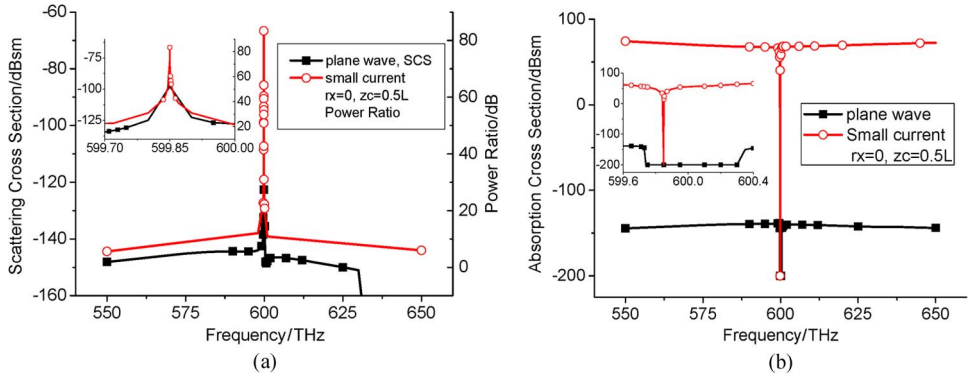

Fig. 18. Comparisons of the results for the plane wave and EHD excitations of the AOC-CNP. (a) SCS versus the PR. (b) ACS.

Consequently, these results further indicate that the EHD does not have to be placed accurately to achieve a significantly enhanced total radiated power.

4.4. Horizontal EHD Excitation

Finally, we considered the AOC-CNP excited by a horizontally oriented EHD. The EHD was located at points D ($rx = -35$ nm, $zc = 0$) and M ($rx = -35$ nm, $zc = L/2$). The predicted PR and ACS results are shown in Fig. 17. One sees immediately that while the resonance still occurs at 599.85 THz, the enhancements are much smaller. The value produced by the EHD located at point M is -0.52 dB smaller than when it is located at point D. The maximum value at point D, 3.03 dB, is much less than the 29.04 dB result for the vertically polarized EHD. Similarly, it is 3.70 dB and 3.41 dB at points O and E. Thus, one finds that the AOC-CNP behavior is very polarization dependent. The enhancements significantly favor the vertical polarization excitation for the current aspect ratio of the geometry.

4.5. Comparisons Between the Planewave and EHD Results

The PR, SCS, and ACS results for the planewave and EHD excitations of the AOC-CNP are compared in Fig. 18. In both cases the resonance frequency is 599.85 THz for the $r1 = 21.3$ nm design. Note that with the EHD excitation and the substrate size, the smallest sphere enclosing this nanoantenna system has the radius $a = 45\sqrt{2}$ nm, giving $ka = 0.8$, i.e., the radiating system is electrically small. The PR at the resonance frequency for the EHD excitation is about 71.3 dB larger than the background value (the PR at 601 THz). In contrast, it is only a 50.03-dBsm

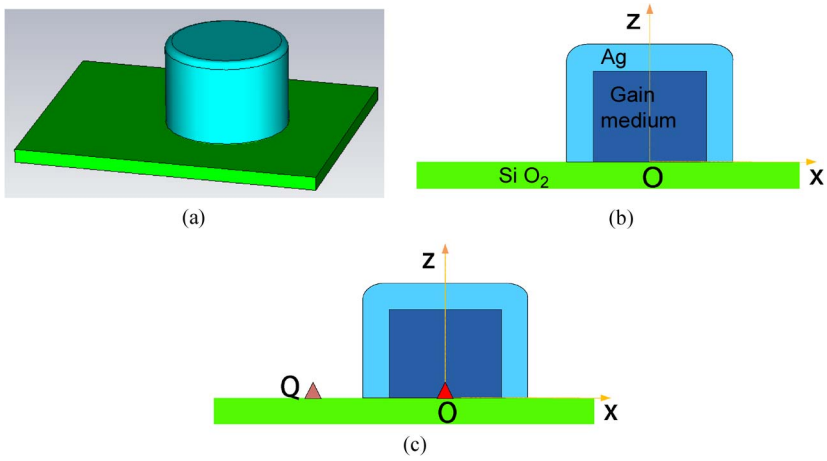

Fig. 19. Asymmetrical AOC-CNP model. (a) Perspective view; (b) material components; and (c) EHD locations. Point O $(rx = 0, zc = 0)$ and Q $(rx = -35\ \text{nm}, zc = 0)$.

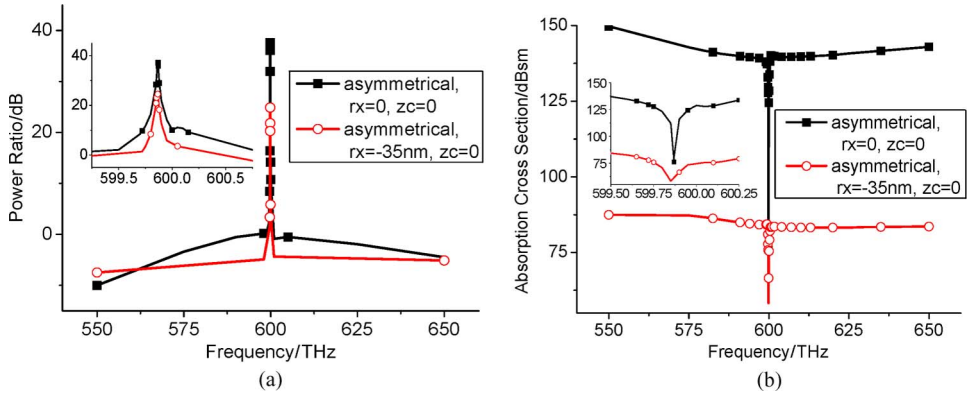

Fig. 20. Results for the asymmetric AOC-CNP. (a) Power ratio values for the EHD located at points O and Q and (b) the corresponding ASC values.

increment of the SCS for the planewave excitation. This difference is due to the fact that the active cylinder is resonant in the near field of the EHD. Consequently, the incident field values are much larger there than the incident planewave (amplitude 1 V/m). Similarly, the ACS dips down to 61.8 dBsm below the relative background value for the plane excitation, while it sinks to 268 dBsm below background for the EHD. Because the Q of the EHD nanoantenna system is much higher than that of its planewave counterpart, the bandwidth for the planewave results, i.e., 0.56 THz, is much larger than its EHD value, i.e., 0.01 THz.

5. Asymmetrical Structure With Vertical EHD Excitation

We also explored an asymmetric structure to acknowledge the fact that during fabrication, the cylinder might not be centered on the silica slab. The asymmetrical substrate AOC-CNP model is shown in Fig. 19. The cylindrical structure and the materials are the same as those reported above. The substrate size is now 135 nm $\times$ 108 nm $\times$ 6 nm. The cylinder (silver thickness $dd = 6.0$ nm, cavity height $L = 31.5$ nm, and radius $r1 = 21.3$ nm) is offset 22.5 nm from the middle of the substrate along the x-axis. As previously, the EHD is implemented as a small current element $(d = 2.0\ \text{nm})$, giving the current moment $I_0\ d = 2 \times 10^{-12}$ A-m and oriented parallel to the z-axis.

The predicted PR and ASC values are shown in Fig. 20. This active nanoantenna is resonant at 599.87 THz, a very slight blue shift. It produces a 37.82-dB maximum PR when the EHD is located at

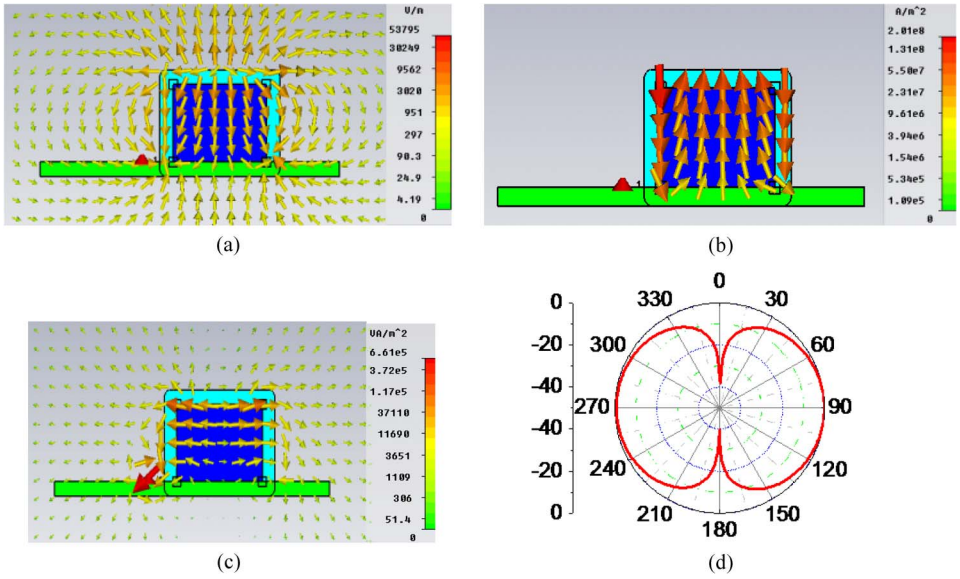

Fig. 21. Simulation results at the resonance at 598.57 THz for the asymmetric AOC-CNP. (a) Electric field, (b) current density, (c) power flow, and (d) far field pattern in the $\phi = 0^\circ$ plane.

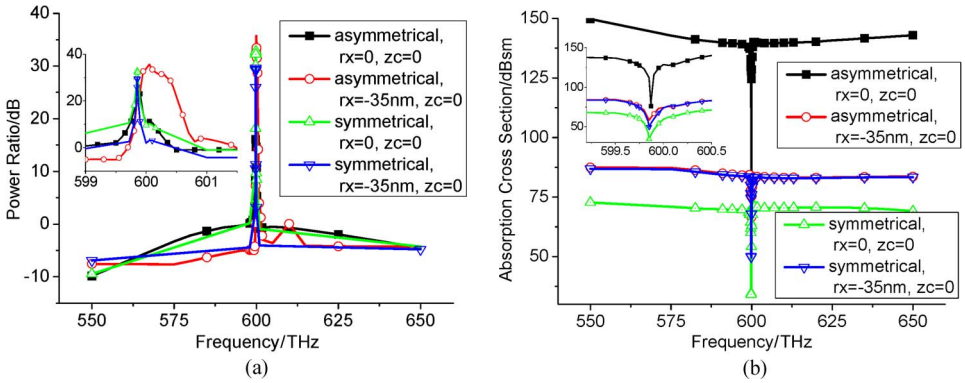

Fig. 22. Comparison of the predicted PR and ACS results for the symmetric and asymmetric AOC-CNPs. (a) Power ratio values for the EHD located at points O and Q and (b) the corresponding ASC values.

point O $(rx = 0, zc = 0)$. The ACS has the expected corresponding behavior; its minimum is at the resonance frequency and is 62.9 dBsm below the background value. The maximum PR and minimum ASC at the resonance frequency when the EHD is located at point Q $(rx = -35\ \text{nm}, zc = 0)$ are, respectively, 24.87 dB and 58.30 dBsm. Plots of the electric field, current density, power flow and directivity pattern at the resonance frequency for the EHD located at point Q are given in Fig. 21. Their behaviors are basically the same as those of the symmetric structure. Again, the AOC-CNP dominates the near- and far-field response of this nanoantenna system; despite the offsets, it produces the fundamental dipole mode behavior.

Direct comparisons of the PR and ASC results for the symmetric and asymmetric structures are given in Fig. 22. The asymmetric structure produces PR values very similar to the symmetric case. It has a PR bandwidth that is slightly larger than the symmetric case; it produces a correspondingly slightly lower maximum. On the other hand, because it has a lower Q and is not as highly tuned, the baseline values of the ACS curves are quite higher than for the symmetric case. In the same manner, the symmetric structure yields a much deeper ACS null than does the asymmetric one.

6. Conclusion

In summary, we have numerically simulated a noncanonical nanoscatterer and nanoantenna structure based on a gain doped SiO_2 core within a highly subwavelength-sized, active open cylindrical CNP that rests on a finite rectangular passive SiO_2 substrate. As with their closed, spherical CNP counterparts, it was demonstrated that these noncanonical open nanostructures can be designed to be resonant and at their resonance frequency, they act as dipole radiators that produce a substantial enhancement of the total radiated power and a corresponding decrease of the ACS. This occurs for either a planewave or an EHD excitation. The PR enhancement relative to the background of the AOC-CNP nanoantenna is about 71.3 dB when the EHD is oriented along the major axis of the cylinder, i.e., vertically. The increment of the SCS relative to the background is about 50.03 dBsm for the related vertically polarized planewave excitation. The corresponding ACS for the nanoantenna (EHD excitation) and nanoscatterer (planewave excitation) has a large negative decrease at resonance indicating significant amplification, i.e., it is, respectively, about 268 dB and 61.8 dB below their relative background values. The vertically polarized EHD excitations produce larger enhancements, but with narrower bandwidths, in comparison with the planewave excitation case. An asymmetric version of the structure was also reported for the EHD excitation. For the vertically oriented EHD, the PR for the symmetrical substrate is larger than that for the asymmetrical substrate case but at a cost of a lower bandwidth. The horizontally polarized EHD excitation of the AOC-CNP was also considered. However, it was shown that the resulting enhancements were significantly smaller than for the vertically polarized excitations. The results demonstrate the AOC-CNP acts as a nanoamplifier and could be used readily for nanoantenna and nanosensor applications.

Acknowledgment

The authors would like to thank S. Campbell, College of Optical Sciences, University of Arizona, for several enlightening technical discussions.

References

[1] B. Garcıá-Cámara, F. Moreno, F. González, and O. J. F. Martin, "Light scattering by an array of electric and magnetic nanoparticles," *Opt. Exp.*, vol. 18, no. 10, pp. 10 001–10 015, May 2010.
[2] J. A. Gordon and R. W. Ziolkowski, "CNP optical metamaterials," *Opt. Exp.*, vol. 16, no. 9, pp. 6692–6716, Apr. 2008.
[3] P. K. Jain, X. Huang, I. H. El-Sayed, and M. A. El-Sayed, "Noble metals on the nanoscale: Optical and photothermal properties and some applications in imaging, sensing, biology, and medicine," *Acc. Chem. Res.*, vol. 41, no. 12, pp. 1578–1586, May 2008.
[4] X. Liu and Q. Huo, "A washing-free and amplification-free one-step homogeneous assay for protein detection using gold nanoparticle probes and dynamic light scattering," *J. Immunol. Methods*, vol. 349, no. 1/2, pp. 38–44, Aug. 2009.
[5] K. R. Catchpole and A. Polman, "Plasmonic solar cells," *Opt. Exp.*, vol. 16, no. 26, pp. 21 793–21 800, Dec. 2008.
[6] R. A. Pala, J. White, E. Barnard, J. Liu, and M. L. Brongersma, "Design of plasmonic thin-film solar cells with broadband absorption enhancements," *Adv. Mater.*, vol. 21, no. 34, pp. 3504–3509, Sep. 2009.
[7] H. A. Atwater and A. Polman, "Plasmonics for improved photovoltaic devices," *Nat. Mater.*, vol. 9, no. 3, pp. 205–213, Mar. 2010.
[8] G. Shvets, S. Trendafilov, J. B. Pendry, and A. Sarychev, "Guiding, focusing, and sensing on the subwavelength scale using metallic wire arrays," *Phys. Rev. Lett.*, vol. 99, no. 5, p. 053903, Aug. 2007.
[9] A. Grbic, L. Jiang, and R. Merlin, "Near-field plates: Subdiffraction focusing with patterned surfaces," *Science*, vol. 320, no. 5875, pp. 511–513, Apr. 2008.
[10] S. Kawata, Y. Inouye, and P. Verma, "Plasmonics for near-field nano-imaging and superlensing," *Nat. Photon.*, vol. 3, no. 7, pp. 388–394, Jul. 2009.
[11] A. W. H. Lin, N. A. Lewinski, J. L. West, N. J. Halas, and R. A. Drezek, "Optically tunable nanoparticle contrast agents for early cancer detection: Model-based analysis of gold nanoshells," *J. Biomed. Opt.*, vol. 10, no. 6, p. 064035, Nov./Dec. 2005.
[12] J. A. Gordon and R. W. Ziolkowski, "Investigating functionalized active coated nano-particles for use in nano-sensing applications," *Opt. Exp.*, vol. 15, no. 20, pp. 12 562–12 582, Oct. 2007.
[13] N. J. Halas, "Plasmonics: An emerging field fostered by Nano Letters," *Nano Lett.*, vol. 10, no. 10, pp. 3816–3822, Oct. 2010.
[14] J. A. Gordon and R. W. Ziolkowski, "The design and simulated performance of a coated nano-particle laser," *Opt. Exp.*, vol. 15, no. 20, pp. 2622–2653, Oct. 2007.
[15] M. I. Stockman, "The spaser as a nanoscale quantum generator and ultrafast amplifier," *J. Opt.*, vol. 12, no. 2, p. 024004, Jan. 2010.

[16] J. A. Gordon and R. W. Ziolkowski, "Colors generated by tunable plasmon resonances and their potential application to ambiently illuminated color displays," *Solid State Commun.*, vol. 146, no. 5/6, pp. 228–238, May 2008.
[17] S. Arslanagi and R. W. Ziolkowski, "Active coated nano-particle excited by an arbitrarily located electric Hertzian dipole—Resonance and transparency effects," *J. Opt.*, vol. 12, no. 2, p. 024014, Feb. 2010.
[18] S. Arslanagi and R. W. Ziolkowski, "Active coated nanoparticles: impact of plasmonic material choice," *Appl. Phys. A*, vol. 103, no. 3, pp. 795–798, Jan. 2011.
[19] S. Arslanagi, R. W. Ziolkowski, and O. Breinbjerg, "Radiation properties of an electric Hertzian dipole located near-by concentric metamaterial spheres," *Radio Sci.*, vol. 42, p. RS6S16, Nov. 2007, DOI:10.1029/2007RS003663.
[20] R. D. Averitt, S. L. Westcott, and N. J. Halas, "Linear optical properties of gold nanoshells," *J. Opt. Soc. Amer. B, Opt. Phys.*, vol. 16, no. 10, pp. 1824–1832, Oct. 1999.
[21] M. A. Noginov, G. Zhu, R. Bakker, V. M. Shalaev, E. E. Narimanov, S. Stout, E. Herz, T. Suteewong, and U. Wiesner, "Demonstration of a spaser-based nanolaser," *Nature*, vol. 460, no. 7259, pp. 1110–1112, Aug. 2009.
[22] E. Desurvire, "Study of the complex atomic susceptibility of erbium-doped fiber amplifiers," *J. Lightw. Technol.*, vol. 8, no. 10, pp. 1517–1527, Oct. 1990.
[23] D. J. Bergman and M. I. Stockman, "Surface plasmon amplification by stimulated emission of radiation: Quantum generation of coherent surface plasmons in nanosystems," *Phys. Rev. Lett.*, vol. 90, no. 2, p. 027402, Jan. 2003.
[24] S. Xiao, V. P. Drachev, A. V. Kildishev, X. Ni, U. K. Chettiar, H. K. Yuan, and V. M. Shalaev, "Loss-free and active optical negative-index metamaterials," *Nature*, vol. 466, no. 7307, pp. 735–738, Aug. 2010.
[25] J. N. Farahani, D. W. Pohl, H. J. Eisler, and B. Hecht, "Single quantum dot coupled to a scanning optical antenna: A tunable superemitter," *Phys. Rev. Lett.*, vol. 95, no. 1, p. 017402, Jan. 2005.
[26] G. Léveque and O. J. F. Martin, "Tunable composite nanoparticle for plasmonics," *Opt. Lett.*, vol. 31, no. 18, pp. 2750–2752, Sep. 2006.
[27] K. H. Su, Q. H. Wei, and X. Zhang, "Tunable and augmented plasmon resonances of Au/SiO_2/Au nanodisks," *Appl. Phys. Lett.*, vol. 88, no. 6, p. 063118, Feb. 2006.
[28] E. Cubukcu, E. A. Kort, K. B. Crozier, and F. Capasso, "Plasmonic laser antenna," *Appl. Phys. Lett.*, vol. 89, no. 9, p. 093120, Aug. 2006.
[29] J. Li, A. Salandrino, and N. Engheta, "Shaping light beams in the nanometer scale: A Yagi-Uda nanoantenna in the optical domain," *Phys. Rev. B, Condens. Matter*, vol. 76, no. 24, p. 245403, Dec. 2007.
[30] J. Zhang, J. Yang, X. Wu, and Q. Gong, "Electric field enhancing properties of the V-shaped optical resonant antennas," *Opt. Exp.*, vol. 15, no. 25, pp. 16 852–16 859, Dec. 2007.
[31] O. L. Muskens, V. Giannini, J. A. Sánchez-Gil, and J. Gómez Rivas, "Optical scattering resonances of single and coupled dimer plasmonic nanoantennas," *Opt. Exp.*, vol. 15, no. 26, pp. 17 736–17 746, Dec. 2007.
[32] R. M. Bakker, A. Boltasseva, Z. Liu, R. H. Pedersen, S. Gresillon, A. V. Kildishev, V. P. Drachev, and V. M. Shalaev, "Near-field excitation of nanoantenna resonance," *Opt. Exp.*, vol. 15, no. 21, pp. 13 682–13 688, Oct. 2007.
[33] M. L. Brongersma, "Engineering optical nanoantennas," *Nat. Photon.*, vol. 2, pp. 270–272, May 2008.
[34] A. Alú and N. Engheta, "Tuning the scattering response of optical nanoantennas with nanocircuit loads," *Nat. Photon.*, vol. 2, pp. 307–310, May 2008.
[35] J. Merlein, M. Kahl, A. Zuschlag, A. Sell, A. Halm, J. Boneberg, P. Leiderer, A. Leitenstorfer, and R. Bratschitsch, "Nanomechanical control of an optical antenna," *Nat. Photon.*, vol. 2, pp. 230–233, Mar. 2008.
[36] H. Fischer and O. J. F. Martin, "Engineering the optical response of plasmonic nanoantennas," *Opt. Exp.*, vol. 16, no. 12, pp. 9144–9154, Jun. 2008.
[37] S. Kuhn, U. Håkanson, L. Rogobete, and V. Sandoghdar, "Enhancement of single-molecule fluorescence using a gold nanoparticle as an optical nanoantenna," *Phys. Rev. Lett.*, vol. 97, no. 1, p. 017402, Jul. 2006.
[38] L. Novotny, "Effective wavelength scaling for optical antennas," *Phys. Rev. Lett*, vol. 98, no. 26, p. 266802, Jun. 2007.
[39] J. Aizpurua, G. W. Bryant, L. J. Richter, F. J. Garcia de Abajo, B. K. Kelley, and T. Mallouk, "Optical properties of coupled metallic nanorods for field-enhanced spectroscopy," *Phys. Rev. B, Condens. Matter Mater. Phys.*, vol. 71, no. 23, p. 235 420, Jun. 2005.
[40] P. Mühlschlegel, H.-J. Eisler, O. J. F. Martin, B. Hecht, and D. W. Pohl, "Resonant optical antennas," *Science*, vol. 308, no. 5728, pp. 1607–1609, Jun. 2005.
[41] T. H. Taminiau, R. J. Moerland, F. B. Segerink, L. Kuipers, and N. F. van Hulst, "$\lambda/4$ resonance of an optical monopole antenna probed by single molecule fluorescence," *Nano Lett.*, vol. 7, no. 1, pp. 28–33, Jan. 2007.
[42] T. H. Taminiau, F. B. Segerink, and N. F. van Hulst, "A monopole antenna at optical frequencies: Single-molecule near-field measurements," *IEEE Trans. Antennas Propag.*, vol. 55, no. 11, pp. 3010–3017, Nov. 2007.
[43] D. P. Fromm, A. Sundaramurthy, P. J. Schuck, G. Kino, and W. E. Moerner, "Gap-dependent optical coupling of single 'bowtie' nanoantennas resonant in the visible," *Nano Lett.*, vol. 4, no. 5, pp. 957–961, Mar. 2004.
[44] O. L. Muskens, V. Giannini, J. A. Sanchez-Gil, and J. Gómez Rivas, "Strong enhancement of the radiative decay rate of emitters by single plasmonic nanoantennas," *Nano Lett.*, vol. 7, no. 9, pp. 2871–2875, Sep. 2007.
[45] L. Rogobete, F. Kaminski, M. Agio, and V. Sandoghdar, "Design of plasmonic nanoantennae for enhancing spontaneous emission," *Opt. Lett.*, vol. 32, no. 12, pp. 1623–1625, Jun. 2007.
[46] A. Alù and N. Engheta, "Hertzian plasmonic nanodimer as an efficient optical nanoantenna," *Phys. Rev. B, Condens. Matter Mater. Phys.*, vol. 78, no. 19, p. 195111, Nov. 2008.
[47] T. H. Taminiau, F. D. Stefani, and N. F. van Hulst, "Enhanced directional excitation and emission of single emitters by a nano-optical Yagi-Uda antenna," *Opt. Exp.*, vol. 16, no. 14, pp. 16 858–16 866, Jul. 2008.
[48] L. Wang, S. M. Uppuluri, E. X. Jin, and X. Xu, "Nanolithography using high transmission nanoscale bowtie apertures," *Nano Lett.*, vol. 6, no. 3, pp. 361–364, Feb. 2006.
[49] A. Sundaramurthy, P. J. Schuck, N. R. Conley, D. P. Fromm, G. S. Kino, and W. E. Moerner, "Toward nanometer-scale optical photolithography: Utilizing the near-field of bowtie optical nanoantennas," *Nano Lett.*, vol. 6, no. 3, pp. 355–360, Mar. 2006.

[50] M. T. Hill, Y.-S. Oei, B. Smalbrugge, Y. Zhu, T. de Vries, P. J. van Veldhoven, F. W. M. van Otten, T. J. Eijkemans, J. P. Turkiewicz, H. de Waardt, E. Geluk, S.-H. Kwon, Y.-H. Lee, R. Nötzel, and M. K. Smit, "Lasing in metallic-coated nanocavities," *Nat. Photon.*, vol. 1, no. 10, pp. 589–594, Sep. 2007.
[51] [Online]. Available: http://www.cst.de/Content/Company/Academic.aspx
[52] T. Weiland, "Time domain electromagnetic field computation with finite difference methods," *Int. J. Numer. Modelling—Electron. Netw., Devices Fields*, vol. 9, no. 4, pp. 295–319, Jul. 1996.
[53] J. Geng, R. W. Ziolkowski, S. Campbell, R. Jin, and X. Liang, "Studies of nanometer antennas incorporating gain material using CST," in *Proc. IEEE AP-S Int. Symp.*, Spokane, WA, Jul. 2011, pp. 1624–1627, Paper 308.10.
[54] P. B. Johnson and R. W. Christy, "Optical constants of the noble metals," *Phys. Rev. B, Condens. Matter Mater. Phys.*, vol. 6, no. 12, pp. 4370–4379, Dec. 1972.
[55] N. W. Ashcroft and N. D. Mermin, *Solid State Physics*. New York: Holt, Rinehart, Winston, 1976.
[56] B. E. A. Saleh and M. C. Teich, *Fundamentals of Photonics*. New York: Wiley, 1991.
[57] C. A. Balanis, *Antenna Theory: Analysis and Design,* 3rd ed. New York: Wiley, 2005.